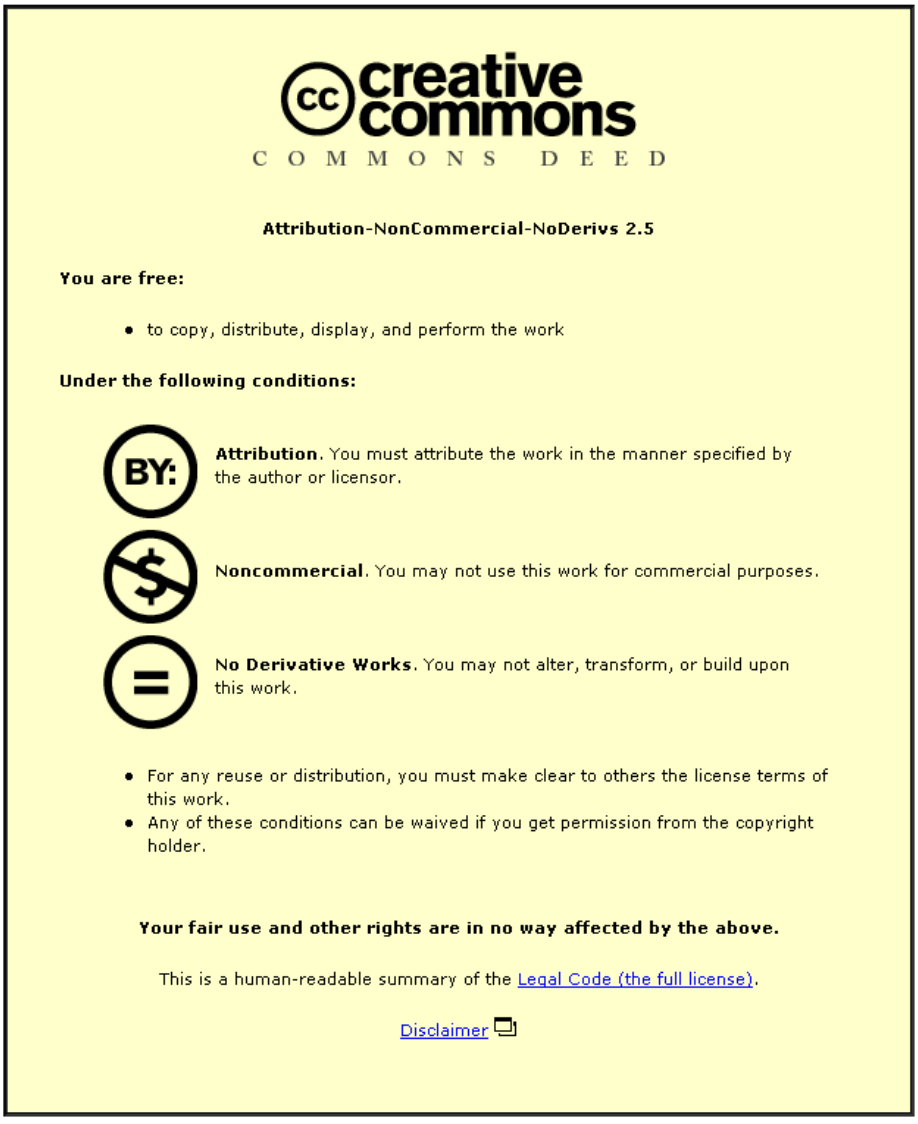

creative commons

COMMONS DEED

Attribution-NonCommercial-NoDerivs 2.5

You are free:

- to copy, distribute, display, and perform the work

Under the following conditions:

Attribution. You must attribute the work in the manner specified by the author or licensor.

Noncommercial. You may not use this work for commercial purposes.

No Derivative Works. You may not alter, transform, or build upon this work.

- For any reuse or distribution, you must make clear to others the license terms of this work.
- Any of these conditions can be waived if you get permission from the copyright holder.

Your fair use and other rights are in no way affected by the above.

This is a human-readable summary of the Legal Code (the full license).

Disclaimer

Published in: Computational Materials Science, 2013.

Indentation studies in b.c.c. crystals with enhanced model of strain-gradient crystal plasticity

Murat Demiral*, Anish Roy, Vadim V. Silberschmidt

Wolfson school of Mechanical and Manufacturing Engineering, Loughborough University, LE11 3TU UK

*Corresponding author. Tel.: +44 1509 227637; Fax: +44 1509 227648
E-mail: M.Demiral@lboro.ac.uk

Abstract

An enhanced model of strain-gradient crystal plasticity is used to study the deformation behaviour of b.c.c. single crystals of a β-Ti alloy under indentation. In this model, both incipient strain gradients, linked to a component's surface-to-volume ratio, and strain gradients evolving in the course of deformation were characterized. The results of numerical simulations are in a good agreement with the obtained experimental data demonstrating an anisotropic nature of surface topographies around the indents performed in different crystallographic orientations. The influence of evolved strain gradients on the surface profile of indents is demonstrated.

1 Introduction and motivation

Metallic samples with a structural dimension of 100 μm and less display a strong size-dependence of their mechanical behaviour with the general trend that smaller is harder [1-3]. Several pioneering experimental studies have identified the existence of a size effect (SE), typically under non-uniform deformation conditions,

http://dx.doi.org/10.1016/j.commatsci.2013.06.057

such as in torsion [4], bending [5] and indentation [1]. From a modelling standpoint, gradient plasticity theories [6-11] that account for the effect of geometrically necessary dislocations (GNDs) [12,13] on plastic flow have had some success in explaining observed size effects.

In the recent past, a size effect in free-standing thin films under homogeneous uniaxial deformation [14,15] and compression of micron- and nano-sized pillars [3] was reported. Numerical results from a finite-element (FE) implementation of a dislocation mechanics-based plasticity theory, namely, Mesoscopic Field Dislocation Mechanics [16,17] were shown to be in a good qualitative agreement with experimental observation [18].

Up to now, different modelling approaches have been proposed to characterise phenomena observed in compression of nano- and micron-sized pillars, such as a source-truncation model [19], a source-exhaustion hardening model [20], multiplication via a single-arm source operation [19,21], a weakest-link theory [22] and a dislocation-starvation/dislocation-nucleation theory [23]. The general premise of these theories is to represent dislocation-source operations in a discrete fashion, where strength of samples is linked to the source lengths. The study of Jennings *et al*. [24], on the other hand, demonstrated that size effects depended on a microstructure rather than a fabrication technique, as was proposed in [25,26]. Maass *et al*. [27] investigated the initial microstructure of undeformed Au, Ni, Cu and NiTi micropillars using a white-beam Laue micro-diffraction technique. This study discovered that strain gradients existed even in the initial microstructure of pillars and their occurrence was proportional to a pillar's surface-to-volume ratio. Motivated by this, Zhang and Aifantis [28] developed a continuum-based strain-gradient model and captured the SE and strain bursts that were successfully experimentally observed in single-crystal Ni micropillars.

It is known that in nano-indentation experiments, deformation of the indented volume of a workpiece material is restricted by the neighbouring material. As the

http://dx.doi.org/10.1016/j.commatsci.2013.06.057

traction-free surfaces are sufficiently away in contrast to surface-dominated samples in micro-pillar-compression experiments, where the studied volumes are not constrained by the surrounding material, the influence of pre-existing strain gradients is not similar in these two test types. This was recently addressed by Demiral *et al*. [29] in a developed enhanced modelling of strain-gradient crystal-plasticity (EMSGCP) theory, where the initial microstructure of micro-pillars determining a value of critical resolved shear stress (CRSS) of slip systems was described in terms of GNDs in addition to statistically stored dislocations (SSDs). The incipient strain gradients were correlated with the sample's surface-to-volume (S/V) ratio. It is worth mentioning that SSDs are dislocations generated by trapping each other in a random way and believed to be dependent on the effective plastic strain [12], whereas GNDs are stored dislocations that relieve plastic-deformation incompatibilities, i.e. strain gradients, within the material caused by non-uniform dislocation slip.

As S/V ratio is negligibly small in nano-indentation samples, the influence of pre-existing strain gradients is insignificant; hence, the CRSS value of slip systems depends on the evolution of SSDs. In this study, nano-indentation tests were carried out for different orientations of a body-centred cubic (b.c.c.) beta phase of Ti-15V-3Al-3Sn-3Cr (in short: Ti-15-3-3-3). Appropriate material parameters were obtained by calibrating a developed three-dimensional finite-element model with the data from experiments. These parameters determine relative contributions of SSDs and GNDs to the CRSS of slip systems in micro-pillar compression samples, where the ratio of S/V is significant and increases with a decreasing pillar's size. Our studies based on micro-pillar experiments will be reported in the future.

This paper is organized as follows. In Section 2, notation conventions are settled. Relevant experimental studies are presented in Section 3. Section 4 describes the theoretical ramifications of the enhanced strain-gradient plasticity framework with the developed finite-element modelling technique. In Section 5 we present some

http://dx.doi.org/10.1016/j.commatsci.2013.06.057

critical results of our nano-indentation studies and their discussion. A case study of micro-pillar compression is demonstrated in Chapter 6. The paper ends with some concluding remarks in Section 7.

2 Notation

A bold symbol denotes a vector or a tensor and a dot superposed on a symbol indicates a material time derivative. The operation × denotes a vector product. The summation convention is implied throughout. A superscript G indicates GNDs and S implies SSDs. A gradient operator is indicated by ∇, and incremental changes in variables due to their temporal evolution are indicated by a Δ symbol.

3 Experimental study

The *ex-situ* nano-indentation experiments with a SEM instrument were performed using a commercial nano-indenter Hysitron UBI equipped with a conical indenter (tip radius: 1 μm; opening angle: 90°). This indenter was selected to avoid symmetries other than those of the crystal structure. Nano-indentation tests were conducted for two different orientations, *viz.* (0.641 0.078 0.764) and (0.114 0.107 0.988), of the single-crystal metastable β-titanium alloy Ti-15-3-3-3. The crystal orientations were determined by electron back-scattering diffraction (EBSD). The maximum indentation load of 6 mN was imposed under a constant loading and unloading rate of 0.1 mN/s.

Post-indentation features such as pile-up heights were characterized with atomic force microscopy (AFM). As seen in Fig. 1, different surface topographies were obtained with the symmetric indenter for the two orientations studied. For the crystal with orientation (0.641 0.078 0.764), a two-fold symmetry was observed, while orientation (0.114 0.107 0.988) resulted in a four-fold symmetry. These differences demonstrated strong crystallographic anisotropy of out-of plane displacements around the indents and can be explained by the differences in

http://dx.doi.org/10.1016/j.commatsci.2013.06.057

intersection vectors of the primary slip planes with the indented surface planes for different crystallographic orientations [30,31].

In b.c.c. crystals slip may occur on 48 individual slip systems in three different sets: 12 slip systems from {110} <111> and {112} <111> families each and 24 slip systems from {123} <111> family. Positions of the pile-up and orientations of slip lines around the imprints are determined by the active slip system. For the β-Ti alloy, Nowag *et al.* [32] compared experimentally observed and theoretically expected positions of the slip bands for all possible glide planes in a grain with different orientations and made some interesting observations. The study suggests that the {112} <111> slip system was dominant during deformation for the investigated grain orientations.

Fig. 1.

4 EMSGCP theory and finite-element modelling of indentation

For convenience, in this section, first a brief self-contained description of governing equations of the EMSGCP theory is presented followed by details of the developed FE model of nano-indentation.

An elasto-visco-plastic crystal plasticity-based constitutive law incorporating strain gradients is used to describe the anisotropic behaviour of a crystal. The constitutive law is based on the Schmid's law, which implies that movement of dislocations, i.e. slip, occurs when the resolved shear stress τ^{α} on a crystallographic plane in the direction of slip reaches a threshold value, known as *critical resolved shear stress* (CRSS) $g_T^{\alpha}|_{t=0}$.

The stress rate, $\dot{\sigma}_{ij}$, is related to the elastic strain rate $\dot{\varepsilon}_{kl}^{\mathrm{e}}$ as:

$$\dot{\sigma}_{ij} = C_{ijkl}\dot{\varepsilon}_{kl}^{\mathrm{e}} = C_{ijkl}\left(\dot{\varepsilon}_{ij} - \dot{\varepsilon}_{kl}^{\mathrm{p}}\right), \tag{1}$$

http://dx.doi.org/10.1016/j.commatsci.2013.06.057

where $\boldsymbol{C}$ is the fourth-order elasticity tensor, $\dot{\varepsilon}_{ij}$ is the total strain rate and $\dot{\varepsilon}^{\mathrm{p}}_{kl}$ is the plastic strain rate, calculated by

$$\dot{\varepsilon}^{\mathrm{p}}_{ij} = \sum_{\alpha=1}^{N} \mu^{\alpha}_{ij} \dot{\gamma}^{\alpha}. \tag{2}$$

In Eq. (2) μ^{α}_{ij} is the Schmid factor and $\dot{\gamma}^{\alpha}$ is the shear strain rate in a slip system α. The viscoplastic power-law expression proposed by Hutchinson [33] and used to describe $\dot{\gamma}^{\alpha}$ is given in the following form:

$$\dot{\gamma}^{\alpha} = \dot{\gamma}^{\alpha}_{o} \operatorname{sgn}(\tau^{\alpha}) \left| \frac{\tau^{\alpha}}{g^{\alpha}_{\mathrm{T}}} \right|^{n}, \qquad \tau^{\alpha} = \sigma_{ij} \mu^{\alpha}_{ij}, \tag{3}$$

where $\dot{\gamma}^{\alpha}_{o}$ is the reference strain rate, n is the rate sensitivity of the material, g^{α}_{T} is the strength of the slip system α at the current time and sgn(■) is the signum function of ■. The main equations of the EMSGCP theory are:

$$g^{\alpha}_{\mathrm{T}} = \sqrt{(g^{\alpha}_{\mathrm{S}}|_{t=0})^2 + (g^{\alpha}_{\mathrm{G}}|_{t=0})^2} + \sqrt{(\Delta g^{\alpha}_{\mathrm{S}})^2 + (\Delta g^{\alpha}_{\mathrm{G}})^2}; \tag{a}$$

$$g^{\alpha}_{\mathrm{T}}|_{t=0} = \mathrm{CRSS} = \sqrt{(g^{\alpha}_{\mathrm{S}}|_{t=0})^2 + (g^{\alpha}_{\mathrm{G}}|_{t=0})^2}; \tag{b}$$

$$g^{\alpha}_{\mathrm{S}}|_{t=0} = K\sqrt{\rho_S|_{t=0}}; \tag{c}$$

$$g^{\alpha}_{\mathrm{G}}|_{t=0} = K\sqrt{\rho_{\mathrm{G}}|_{t=0}} = K\sqrt{\rho|_{t=0}\left(\frac{\bar{S}}{\bar{V}}\right)^2}; \tag{d}$$

$$\Delta g^{\alpha}_{\mathrm{S}} = \sum_{\beta=1}^{N} h_{\alpha\beta} \Delta\gamma^{\beta}, \quad \Delta g^{\alpha}_{\mathrm{G}} = \alpha_{\mathrm{T}} \mu \sqrt{b n^{\alpha}_{\mathrm{G}}}. \tag{e}$$

(4)

In the theory the initial strength of the slip systems ($g^{\alpha}_{\mathrm{T}}|_{t=0}$) is governed by pre-existing GNDs in the workpiece together with SSDs (Eq. (4b)), whereas in the mechanism-based strain-gradient crystal-plasticity (MBSGCP) theory [11,34], the CRSS is determined by SSDs only. The evolution of slip resistance during loading, on the other hand, is the resultant of incremental hardening due to both SSDs ($\Delta g^{\alpha}_{\mathrm{S}}$)

http://dx.doi.org/10.1016/j.commatsci.2013.06.057

and GNDs ($\Delta g_{\mathrm{G}}^{\alpha}$) on the slip system α as described in Eq. (4a), identical to that of the MBSGCP theory. In Eq. (4e) $h_{\alpha\beta}$, α_{T}, μ, b and n_{G}^{α} correspond to the hardening matrix, the Taylor coefficient, the shear modulus, the Burgers vector and the effective number density of GNDs at the current time, respectively. It should be emphasized that in the EMSGCP theory $g_{\mathrm{S}}^{\alpha}|_{t=0}$ and $g_{\mathrm{G}}^{\alpha}|_{t=0}$ were correlated with the $\rho_{\mathrm{S}}|_{t=0}$ and $\rho_{\mathrm{G}}|_{t=0}$ via the constant K (Eqs. (4c) and (4d)), similar to the Taylor equation, and the latter density term was expressed as a function of the normalized surface-to-volume ratio (hence unitless) for the component under study (Eq. (4d)) [29]. Such a relationship was established based on the experimental study of Maass *et al*. [27], where it was observed that a higher surface-to-volume ratio in micropillars increased the occurrence of pre-existing GNDs. Thus, the smaller the radii of pillar, the higher is the density of GNDs and, consequently, the higher is the pillar's strength. A reasonable match between the experiments and simulations for different size of micropillars using the EMSGCP theory was obtained [29]. This theory is consistent with the model proposed by Hurtado and Ortiz [35], where surface effects are accounted for in the crystal-plasticity theory.

The hardening moduli $h_{\alpha\beta}$ in Eq. (4e) are evaluated as follows [36]:

$$h_{\alpha\alpha} = h_0 \operatorname{sech}^2 \left| \frac{h_0 \gamma}{g_{\mathrm{T}}^{\alpha}|_{\mathrm{sat}} - g_{\mathrm{T}}^{\alpha}|_{t=0}} \right|, \qquad \text{(a)}$$

$$h_{\alpha\beta} = q h_{\alpha\alpha} (\alpha \neq \beta), \qquad \gamma = \sum_{\alpha} \int_0^t |\dot{\gamma}^{\alpha}| dt\,, \qquad \text{(b)} \tag{5}$$

where h_0 is the initial hardening parameter, $g_{\mathrm{T}}^{\alpha}|_{\mathrm{sat}}$ is the saturation stress of the slip system α at the current time, q is the latent hardening ratio and γ is the cumulative shear strain on all slip systems. The effective density of GNDs (n_{G}^{α}) in Eq. (4e) is obtained from

$$n_{G}^{\alpha} = \left| \boldsymbol{m}^{\alpha} \times \sum_{\beta} s^{\alpha\beta} \nabla \gamma^{\beta} \times \boldsymbol{m}^{\beta} \right|, \tag{6}$$

http://dx.doi.org/10.1016/j.commatsci.2013.06.057

where $\boldsymbol{m}^{\alpha}$ is the slip plane normal, $\boldsymbol{s}^{\alpha}$ is the slip direction with $s^{\alpha\beta} = \boldsymbol{s}^{\alpha}.\boldsymbol{s}^{\beta}$, and $\nabla\gamma^{\beta}$ is the gradient of shear strain in each slip system. The EMSGCP theory was implemented in the implicit general-purpose finite-element code ABAQUS/Standard using the user-defined subroutines UMAT to represent the material response and URDFIL to read the results file during the simulation. An important point in the implementation is the determination of a shear strain gradient $\nabla\gamma^{\beta}$ in Eq. (6). To compute this, first the shear strain values for each slip system, α, at each node within an element were obtained using URDFIL. Next, these data were transferred to the UMAT to compute the shear strain gradients at each integration point using the scheme described by Busso and co-workers [37], where the spatial derivatives of the linear shape functions were calculated. Relevant details can be found in [34, 37, 38].

It is to be noted that the EMSGCP theory reduces to MBSGCP when $g_{\mathrm{G}}^{\alpha}|_{t=0}$ vanishes and to the crystal-plasticity (CP) theory when both $g_{\mathrm{G}}^{\alpha}|_{t=0}$ and $\Delta g_{\mathrm{G}}^{\alpha}$ are zero.

A schematic of the developed indentation model is shown in Fig. 2. Dimensions of the workpiece used in the FE model were 10 μm × 10 μm × 6 μm. A refined mesh with a minimum element size of 100 nm in the vicinity of the indenter's tip and a coarser mesh for the remaining region were used to discretize the workpiece sample, which resulted in 5488 eight-node linear brick elements (C3D8) in total (Fig. 2b). The diamond indenter used in the experiments was modelled as a rigid body. The relative movement of the workpiece and indenter was monitored by the translation of the latter in the negative y-direction with a maximum indentation depth of 375 nm followed by a complete unloading. Kinematic boundary conditions were imposed on the bottom face of the workpiece by constraining displacements in all directions, whereas the faces of the workpiece perpendicular to x- and z-directions were constrained in x- and z-direction, respectively, and the top face was free to deform. The Coulomb's friction law with the coefficient of friction

http://dx.doi.org/10.1016/j.commatsci.2013.06.057

$\mu = 0.05$ was used to model frictional interaction between the indenter and the surface of the workpiece material. Prior studies indicate that the likely values of coefficient of friction between diamond-metal surface interface in microcompression experiments are in the range $0.03 \leq \mu \leq 0.06$ [39].

Fig. 2.

5 Identification of material parameters using nano-indentation experiments

In nano-indentation experiments the surface-to-volume ratio of the indented workpiece is negligibly small, which, in turn, leads to vanishing levels of incipient surface GNDs. The CRSS for a slip system, therefore, is governed only by the contribution of SSDs, i.e. $\text{CRSS} = g_S^\alpha|_{t=0}$. Relative contributions of SSDs and GNDs to the CRSS under macroscopically homogeneous deformation modes may be determined with micro-pillar compression tests [3] and thin-film plane-stress bulge tests [15].

The material parameters in the EMSGCP were obtained by calibrating the developed numerical model with nano-indentation experiments comparing load-displacement curves (*F-d*) and surface profiles (*SP*) of the single-crystal Ti alloy indented in (0.641 0.078 0.764) orientation.

First, the sensitivity of numerical results to the material parameters $\boldsymbol{C}$, n, α_T, τ_0 and τ_s were studied. For instance, it is observed that an increase in τ_0 for fixed elastic constants leads to a "sink-in" in the surface profile as the ratio (of elastic modulus to yield strength) varies from infinity representing rigid-plastic deformation to zero representing elastic deformation [36]. Consequently, an increase in τ_0 for a fixed magnitude of τ_s leads to formation of "pile-up" as a smaller value of $(\tau_\mathrm{s} - \tau_0)$ represents a lower hardening capability of the material under deformation [37-39]. Further details are available in [29].

http://dx.doi.org/10.1016/j.commatsci.2013.06.057

The influence of strain gradients evolved during an inhomogeneous deformation process is critical for accurate characterization of surface profiles during and after the indentation process. As this, to the authors' knowledge, was not addressed in the literature yet, sensitivity of the strain gradients was analysed by varying the Taylor factor, α_T. In our study, three different values of α_T were considered, viz. 0.0, 0.7 and 1.5. Here, α_T = 0.0 means an absence of the strain-gradient effect, essentially implying the CP theory. The material parameters presented in Table 1 were used in simulations. Fig. 3 demonstrates that with an increase in α_T, the pile-up height decreases with an increase in the elastic spring-back of the material. The explanation for this is that in an indentation process rapid spatial changes occur in the local texture evolution due to imposed boundary conditions, which, in turn, lead to mismatches in the lattice spin for portions of neighbouring material [40]. As this is accounted for in the constitutive descriptions of EMSGCP theory by accommodating the evolved GNDs, the surface profile is predicted to be smoother when compared to the predictions from the CP theory, Additionally, with an increase in α_T, the material's effective internal strength increases, leading, in turn, to a well-annealed softer response of the material beyond the yield point. As a result, the amount of spring back increases and the pile-up height decreases simultaneously when the evolved strain gradients are accentuated in the model, i.e. with increasing α_T.

Fig. 3.

Table 1:

A numerical indentation experiment was carried out on a grain of (0.641 0.078 0.764) orientation. All material parameters used are presented in Table 1 [29]. A two-fold symmetry on the indented surface (Fig. 4a) was observed in simulations, as in the experiments (Fig. 1a). A corresponding load-displacement graph (Fig. 5a) and the surface profile of the indented surface along the path A-B in Fig. 6a

http://dx.doi.org/10.1016/j.commatsci.2013.06.057

demonstrate a reasonable match with the obtained experimental data. This implies that the model's calibration process was performed appropriately. To validate the numerical model, simulations were also implemented by indenting a grain with another orientation – (0.114 0.107 0.988). Here, a four-fold symmetry on the surface (Fig. 4b) was observed, which resembled that in the conducted experiments (Fig. 1b). Also, a reasonably good agreement between experiments and simulations was achieved for the obtained *F-d* (Fig. 5b) and *SP* (Fig. 6b) curves, providing a further confirmation on the appropriateness of the selected material's parameters. It must be noted that as the experimentally obtained surface profiles were not scanned with an ideally sharp AFM indenter tip, the holes were imaged sharper, whereas, the peak points were imaged blunter. It is well known that the one of the major ambiguities in AFM imagining arises from the tip shape [41]. This effect somewhat explains the differences in the experimentally and numerically obtained surface profiles.

Fig. 4.

Nano-indentation of single crystals has been studied extensively; however, a comprehensive theoretical framework of small-scale plasticity, which is able to capture all experimentally observed features, is still elusive. For instance, Wang *et al*. [30] studied an effect of crystallographic orientation on pile-up patterns and micro-textures using a CP FE model for single-crystal copper. A correct numerical

Fig. 5.

prediction of the surface pile-up patterns was achieved; however, a deviation by an order of a magnitude in the load-displacement curve between experiments and simulations was reported. Liu *et al*. [38] performed a similar study using a spherical indenter instead of a conical one, where satisfactory agreements between the numerical and experimental load-displacement curves were demonstrated.

http://dx.doi.org/10.1016/j.commatsci.2013.06.057

However, different magnitudes of the coefficient of friction were used to represent the contact condition between the indenter's tip and the workpiece material for different orientations to match numerically obtained surface profiles with the experimental data. Still, an error of up to 50% was reported for the maximum pile-up. In the present study, where both the incipient and evolving strain gradients were considered in the calibration procedure (unlike prior studies), a maximum error of 5% in the load-displacement curve and 18% in the maximum pile-up height was obtained. We refrained from varying the coefficient of friction, which is not physical; instead, we resort to accounting for the intrinsic strain gradients in the constitutive equations of the proposed theory.

Fig. 6.

Fig. 7 presents the relationship between the hardness and the indentation depth predicted by EMSGCP, MBSGCP and CP theories. In this plot, the hardness was computed as $P_{\max}/A_{\text{proj}}$, where $P_{\max}$ is the maximum indentation load and A_{proj} is the projected contact area between the indenter and the workpiece material at $P_{\max}$. In the calculation of A_{proj} the Abaqus output variable COPEN (contact opening distance) with a threshold value of 10^{-5} was used to define the boundary of the contact [38], where the area within the boundary was computed employing Plot Digitizer 2.4.1 [46]. The computed hardness values in the first 100 nm of indentation were ignored since the underlying mesh spacing formed a large fraction of the contact area, which could induce significant errors in the results [47].

It was observed that with an increase in the indentation depth, the hardness increased. The hardness values predicted using the CP theory were found to be lower compared to predictions based on gradient-plasticity theories. The obtained results are consistent with the experiments performed by Swadener [48] as well as the numerical and analytical models proposed in [38], [49], respectively. Both strain gradient theories predict the same hardness values due to a negligible

http://dx.doi.org/10.1016/j.commatsci.2013.06.057

surface-to-volume magnitude. Contribution of SSDs to the CRSS of slip systems can be characterized using indentation studies. This allows assessment of the relative contributions of SSDs and GNDs in surface-dominated structures such as micro-pillar compression samples, where the ratio of S/V is significant, using the EMSGCP theory. To this end, a micro-pillar compression study is presented in the next section.

Fig. 7.

6 Micro-pillar compression study

In this section a three-dimensional FE model of micropillar-compression experiment is developed for two pillars, where the respective diameters were 1 μm (pillar X) and 2 μm (pillar Y) with a constant aspect-ratio (height-to-diameter) of 2.5 (Fig. 8), using the proposed theory to investigate the size effect in a single crystal (010) Ti-based alloy.

The relative movement of the workpiece and indenter was introduced as translation of the latter in the negative y-direction, with the pillars compressed up to 20% of their respective heights. Kinematic boundary conditions were imposed on the bottom face of the pillars by constraining displacements in all directions to represent a tight bond with the substrate [3]. The element size was kept constant for both pillars, as the distribution of GNDs was found to be mesh-size dependent [29, 50].

As the micro-pillars are surface-dominated structures, the contribution of pre-existing GNDs to the CRSS is not negligibly small in contrast to that in nano-indentation tests. The values of parameters $g_{\mathrm{G}}^{\alpha}|_{\mathrm{t}=0}$ and $g_{\mathrm{T}}^{\alpha}|_{\mathrm{t}=0}$ for each pillar were calculated using Eqs. (4d) and (4b), respectively. The respective values are presented in Table 2, where $\rho|_{\mathrm{t}=0}$ was assumed to be 10^6 mm^{-2}. As before, the surface-to-volume ratio of the pillars was normalised with that for the ideal pillar,

http://dx.doi.org/10.1016/j.commatsci.2013.06.057

i.e. $S/V = 1\ \mu m^{-1}$. In the calculation, the pillar surface consists of the top and side surfaces (the bottom surface is neglected since it is bonded to a substrate).

Fig. 8.

Table 2:

Fig. 9 presents the obtained effective stress-strain curves for both pillars using EMSGCP, MBSGCP and CP theories. Here, the effective magnitudes of stress and strain are defined as $|\sum RF_2|/A_p$ and $-\ln(L_p/L_0)$, respectively, where $|\sum RF_2|$ corresponds to the reaction force in the y-direction corresponding to the direction of the applied displacement, A_p is the mid-height-instantenous cross-sectional area of the pillar, and L_p and L_0 corresponds to current and initial height of the pillar, respectively.

It was observed that the magnitude of stress values for pillar X were larger compared to that of the pillar Y at the yield point as well as in the post-elastic regime. The results based on the EMSGCP theory demonstrate that smaller pillars are stronger compared to larger ones, consistent with the experimental observations in the literature [3]. For comparison, the simulations were also carried out using the MBSGCP and CP theories (Fig. 9). As expected, the CP case shows no size effects. For MBSGCP, lower yield strength and stress values in the post-elastic regime were obtained for both pillars. The size effect for the two pillars is somewhat meagre in comparison to EMSGCP.

Fig. 9.

7 Concluding remarks

In this paper, a numerical implementation of an enhanced model of strain-gradient crystal plasticity was used to demonstrate predictive capabilities of the theory in

http://dx.doi.org/10.1016/j.commatsci.2013.06.057

characterizing the surface profiles and macro-scale load-displacement response of b.c.c. single crystals of β-Ti alloy under indentation.

The model parameters were calibrated with the help of nano-indentation experiments. The model accounts for incipient surface GNDs, which arise in small-sized components with non-negligible surface-to-volume ratios. These parameters help to determine relative contributions of SSDs and GNDs to the CRSS of slip systems in micro-pillar compression samples, where the ratio of S/V is significant and increases with a decrease in the pillar size. Size effects in components under macroscopic homogeneous deformation modes using EMSGCP theory will be discussed extensively in a future publication.

This study also suggests that accounting for strain gradients evolved during deformation allows for less pronounced surfaces profile of indents as the resulting mismatch in the lattice spin of neighbouring material is accommodated by the evolving local GNDs.

Acknowledgement

Authors would like to acknowledge Kai Nowag from Laboratory for Materials Technology, EMPA, Swiss Federal Laboratories for Materials Testing and Research for providing the experimental data for nano-indentation of the studied Ti-based alloy. The research leading to these results received funding from the European Union Seventh Framework Programme (FP7/2007-2013) under grant agreement No. PITN-GA-2008-211536, project MaMiNa. MD acknowledges the use of the UMAT for the CP theory developed by Yonggang Huang [51] and Jeffrey Kysar [52].

http://dx.doi.org/10.1016/j.commatsci.2013.06.057

References

[1] N. Stelmashenko, M. Walls, L. Brown, Y.V. Milman, Microindentations on W and Mo oriented single crystals: an STM study, Acta Metallur. Mater. 41 (1993) 2855-2865.

[2] K. McElhaney, J. Vlassak, W. Nix, Determination of indenter tip geometry and indentation contact area for depth-sensing indentation experiments, J. Mater. Res. 13 (1998) 1300-1306.

[3] J.R. Greer, J.T.M. De Hosson, Plasticity in small-sized metallic systems: Intrinsic versus extrinsic size effect, Prog. Mater. Sci. 56 (2011) 654-724.

[4] N.A. Fleck, G.M. Muller, M.F. Ashby, J.W. Hutchinson, Strain gradient plasticity: Theory and experiment, Acta Metallur. Mater. 42 (1994) 475-487.

[5] J. Stölken, A. Evans, A microbend test method for measuring the plasticity length scale, Acta Mater. 46 (1998) 5109-5115.

[6] A. Acharya, A. Beaudoin, Grain-size effect in viscoplastic polycrystals at moderate strains, J. Mech. Phys. Solids 48 (2000) 2213-2230.

[7] N. Fleck, J. Hutchinson, A reformulation of strain gradient plasticity, J. Mech. Phys. Solids. 49 (2001) 2245-2271.

[8] H. Gao, Y. Huang, W. Nix, Modeling plasticity at the micrometer scale, Naturwiss. 86 (1999) 507-515.

[9] M.E. Gurtin, On the plasticity of single crystals: free energy, microforces, plastic-strain gradients, J. Mech. Phys. Solids 48 (2000) 989-1036.

http://dx.doi.org/10.1016/j.commatsci.2013.06.057

[10] Y. Huang, H. Gao, W. Nix, J. Hutchinson, Mechanism-based strain gradient plasticity-II. Analysis, J. Mech. Phys. Solids 48 (2000) 99-128.

[11] C. Han, H. Gao, Y. Huang, W.D. Nix, Mechanism-based strain gradient crystal plasticity—I. Theory, J. Mech. Phys. Solids 53 (2005) 1188-1203.

[12] M. Ashby, The deformation of plastically non-homogeneous materials, Phil. Mag. 21 (1970) 399-424.

[13] H. Gao, Y. Huang, Geometrically necessary dislocation and size-dependent plasticity, Scr. Mater. 48 (2003) 113-118.

[14] H. Espinosa, B. Prorok, B. Peng, Plasticity size effects in free-standing submicron polycrystalline FCC films subjected to pure tension, J. Mech. Phys. Solids 52 (2004) 667-689.

[15] Y. Xiang, J. Vlassak, Bauschinger and size effects in thin-film plasticity, Acta Mater. 54 (2006) 5449-5460.

[16] A. Acharya, A. Roy, Size effects and idealized dislocation microstructure at small scales: Predictions of a Phenomenological model of Mesoscopic Field Dislocation Mechanics: Part I, J. Mech. Phys. Solids 54 (2006) 1687-1710.

[17] A. Acharya, A. Roy, A. Sawant, Continuum theory and methods for coarse-grained, mesoscopic plasticity, Scr. Mater. 54 (2006) 705-710.

[18] S. Puri, A. Roy, Plastic deformation of multicrystalline thin films: Grain size distribution vs. grain orientation, Comput. Mater. Sci. 52 (2012) 20-24.

[19] T.A. Parthasarathy, S.I. Rao, D.M. Dimiduk, M.D. Uchic, D.R. Trinkle, Contribution to size effect of yield strength from the stochastics of dislocation source lengths in finite samples, Scr. Mater. 56 (2007) 313-316.

http://dx.doi.org/10.1016/j.commatsci.2013.06.057

[20] D.M. Norfleet, D.M. Dimiduk, S.J. Polasik, M.D. Uchic, M.J. Mills, Dislocation structures and their relationship to strength in deformed nickel microcrystals, Acta Mater. 56 (2008) 2988-3001.

[21] S.I. Rao, D.M. Dimiduk, T.A. Parthasarathy, M.D. Uchic, M. Tang, C. woodward, Athermal mechanisms of size-dependent crystal flow gleaned from three-dimensional discrete dislocation simulations, Acta Mater. 56 (2008) 3245-3259.

[22] J.A. El-Awady, M. Wen, N.M. Ghoniem, The role of the weakest-link mechanism in controlling the plasticity of micropillars, J. Mech. Phys. Solids 57 (2009) 32-50.

[23] J.R. Greer, W.D. Nix, Nanoscale gold pillars strengthened through dislocation starvation, Phys. Rev. B. 73 (2006) 245410.

[24] A.T. Jennings, M.J. Burek, J.R. Greer, Microstructure versus size: Mechanical properties of electroplated single crystalline Cu nanopillars, Phys. Rev. Lett. 104 (2010) 135503.

[25] H. Bei, S. Shim, M. Miller, G. Pharr, E. George, Effects of focused ion beam milling on the nanomechanical behavior of a molybdenum-alloy single crystal, Appl. Phys. Lett. 91 (2007) 111915.

[26] D. Kiener, C. Motz, M. Rester, M. Jenko, G. Dehm, FIB damage of Cu and possible consequences for miniaturized mechanical tests, Mater. Sci. Eng. A. 459 (2007) 262-272.

[27] R. Maass, S. Van Petegem, J. Zimmermann, C. Borca, H. Van Swygenhoven, On the initial microstructure of metallic micropillars, Scr. Mater. 59 (2008) 471-474.

http://dx.doi.org/10.1016/j.commatsci.2013.06.057

[28] X. Zhang, K. Aifantis, Interpreting strain bursts and size effects in micropillars using gradient plasticity, Mater. Sci. Eng. A 528 (2011) 5036–5043.

[29] M. Demiral, Enhanced gradient crystal-plasticity study of size effects in b.c.c. metal, PhD thesis, Loughborough University, UK (2012).

[30] Y. Wang, D. Raabe, C. Klüber, F. Roters, Orientation dependence of nanoindentation pile-up patterns and of nanoindentation microtextures in copper single crystals, Acta Mater. 52 (2004) 2229-2238.

[31] Y. Liu, B. Wang, M. Yoshino, S. Roy, H. Lu, R. Komanduri, Combined numerical simulation and nanoindentation for determining mechanical properties of single crystal copper at mesoscale, J. Mech. Phys. Solids 53 (2005) 2718-2741.

[32] K. Nowag, R. Ghisleni, J. Michler, Effect of crystal orientation on slip-band formation and deformation of a bcc titanium alloy. Laboratory for Materials Technology, EMPA, Swiss Federal Laboratories for Materials Testing and Research (unpublished results).

[33] J. Hutchinson, Bounds and self-consistent estimates for creep of polycrystalline materials, Proc. of the Royal Soc. of London. A. Math. Phys. Sci. 348 (1976) 101-127.

[34] A. Siddiq, S. Schmauder, Y. Huang, Fracture of bicrystal metal/ceramic interfaces: A study via mechanism-based strain gradient crystal plasticity theory, Int. J. Plas. 23 (2007) 665-689.

[35] D.E. Hurtado, M. Ortiz, Surface effects and the size-dependent hardening and strengthening of nickel micropillars, J. Mech. Phys. Solids 60 (2012) 1432-1446.

[36] D. Peirce, R. Asaro, A. Needleman, An analysis of nonuniform and localized deformation in ductile single crystals, Acta Metallur. 30 (1982) 1087-1119.

http://dx.doi.org/10.1016/j.commatsci.2013.06.057

[37] E.P. Busso, F.T. Meissonnier, N.P. O'Dowd, Gradient-dependent deformation of two-phase single crystals, J. Mech. Phys. Solids 48 (2000) 2333-2361.

[38] W.B. Lee, Y.P. Chen, Simulation of micro-indentation hardness of FCC single crystals by mechanism-based strain gradient crystal plasticity, Int. J. Plast. 26 (2010) 1527-1540.

[39] H. Zhang, B.E. Schuster, Q. Wei, K.T. Ramesh, The design of accurate micro-compression experiments, Scr. Mater. 54 (2006) 181-186.

[40] K.L. Johnson, Contact Mechanics, Cambridge University Press, Cambridge (1985).

[41] B. Taljat, G. Pharr, Development of pile-up during spherical indentation of elastic–plastic solids, Int. J. Solids Structures 41 (2004) 3891-3904.

[42] Y. Liu, S. Varghese, J. Ma, M. Yoshino, H. Lu, R. Komanduri, Orientation effects in nanoindentation of single crystal copper, Int. J. Plast. 24 (2008) 1990-2015.

[43] A.F. Gerday, M. Ben Bettaieb, L. Duchêne, N. Clément, H. Diarra, A. Habraken, Interests and limitations of nanoindentation for bulk multiphase material identification: Application to the β phase of Ti-5553, Acta Mater. 57 (2009) 5186-5195.

[44] N. Zaafarani, D. Raabe, R. Singh, F. Roters, S. Zaefferer, Three-dimensional investigation of the texture and microstructure below a nanoindent in a Cu single crystal using 3D EBSD and crystal plasticity finite element simulations, Acta Mater. 54 (2006) 1863-1876.

http://dx.doi.org/10.1016/j.commatsci.2013.06.057

[45] T. Altebaeumer, B. Gotsmann, A. Knoll, G. Cherubini, U. Duerig, Self-similarity and finite-size effects in nano-indentation of highly cross-linked polymers, Nanotech. 19 (2008) 475301.

[46] J.A. Huwaldt. Plot Digitizer 2.4.1, Free software distributed from <http://sourceforge.net/projects/plotdigitizer> (2005).

[47] E. Bittencourt, Numerical solution of crystal plasticity problems by a mixed formulation, Comput. Mater. Sci. 63 (2012) 145-153.

[48] J.G. Swadener, E.P. George, G.M. Pharr, The correlation of the indentation size effect measured with indenters of various shapes, J. Mech. Phys. Solids 50 (2002) 681-694.

[49] Z. Xue, Y. Huang, K.C. Hwang, M. Li, The influence of indenter tip radius on the micro-indentation hardness, J. Eng. Mater. Techol.-Trans. ASME 124 (2002) 371-379.

[50] K.S. Cheong, E.P. Busso, A. Arsenlis, A study of microstructural length scale effects on the behaviour of FCC polycrystals using strain gradient concepts, Int. J. Plast. 21 (2005) 1797-1814.

[51] Y. Huang, A user-material subroutine incorporating single crystal plasticity in the ABAQUS finite element program, Mech Report. 178 (1991).

[52] J. Kysar, Addendum to ‘A user-material subroutine incorporating single crystal plasticity in the ABAQUS finite element program: Mech Report 178', Division of Engineering and Applied Sciences, Harvard University, Cambridge, MA (1997).

http://dx.doi.org/10.1016/j.commatsci.2013.06.057

Table and Figure captions

Table 1: Material parameters for Ti alloy single-crystal micro-pillars used in model development for nano-indentation experiment

Table 2: Material parameters for Ti alloy single-crystal micro-pillars X and Y

Fig. 1. Pile-up structures of imprints obtained with AFM-topography measurement for different crystallographic orientations at complete unloading: (a) (0.641 0.078 0.764) surface; (b) (0.114 0.107 0.988) surface

Fig. 2. Dimensions of indenter and workpiece (in μm) (a); 3D finite-element model of nano-indentation

Fig. 3. Pile-up profiles of indents along path A-B (see Fig. **2**1a) for different α_T values at full loading and complete unloading

Fig. 4. Pile-up structures of imprints obtained from FE simulations for different crystallographic orientations at complete unloading: (a) (0.641 0.078 0.764) surface; (b) (0.114 0.107 0.988) surface

Fig. 5. Load-displacement curves for nano-indentation of (0.641 0.078 0.764) surface (a) and (0.114 0.107 0.988) surface (b) obtained from experiments and simulations at complete unloading

Fig. 6. Pile-up profiles of indented (0.641 0.078 0.764) surface along path A-B (a) and indented (0.579 0.417 0.702) surface along path C-D (b) obtained from experiments and simulations at complete unloading

Fig. 7. Hardness values of indented (0.641 0.078 0.764) surface obtained from simulations using EMSGCP, MBSGCP and CP theories at full loading

http://dx.doi.org/10.1016/j.commatsci.2013.06.057

Fig. 8. The FE method mesh geometries for the pillars X and Y

Fig. 9. Average stress-strain curves for pillars X and Y obtained with FE simulations using EMSGCP, MBSGCP and CP theories

http://dx.doi.org/10.1016/j.commatsci.2013.06.057

TABLES

Table1

Elastic constants	CP parameters	Additional EMSGCP parameters
$C_{11} = 127.740$ GPa	$\dot{\gamma}_o^\alpha = 10^{-4}\ s^{-1}$	$\alpha_T = 0.7$
$C_{12} = 118.850$ GPa	$n = 15$	$K = 0.0392$ MPa. mm
$C_{44} = 43.997$ GPa	$q = 1$	$\mu_s = 13.980$ GPa
	$h_0 = 10000$ MPa	$b = 2.803 \times 10^{-7}$ mm
		$g_T^\alpha\|_{t=0} \approx g_S^\alpha\|_{t=0} = 150$ MPa
		$g_T^\alpha\|_{t=sat} \approx g_S^\alpha\|_{t=sat} = 170$ MPa

Table2

Pillar	$\bar{S}/\bar{V}$	$g_S^\alpha\|_{t=0}$ (MPa)	$g_G^\alpha\|_{t=0}$ (MPa)	$g_T^\alpha\|_{t=0}$ (MPa)	$g_T^\alpha\|_{sat}$ (MPa)
X	4.4	150	172.44	228.55	248.55
Y	2.2	150	86.22	173.01	193.01

http://dx.doi.org/10.1016/j.commatsci.2013.06.057

FIGURES

Fig1.

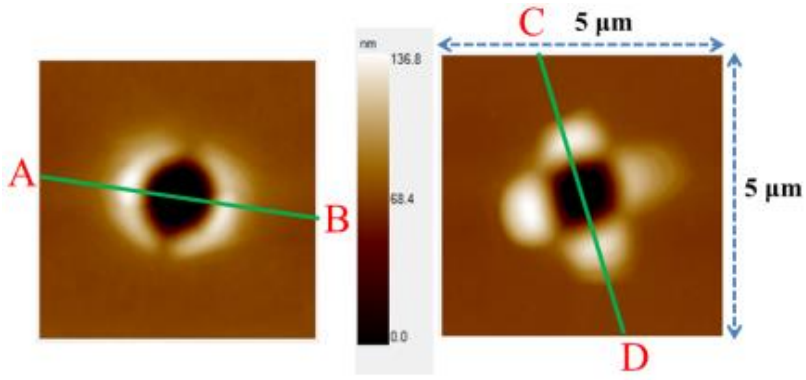

Fig.2

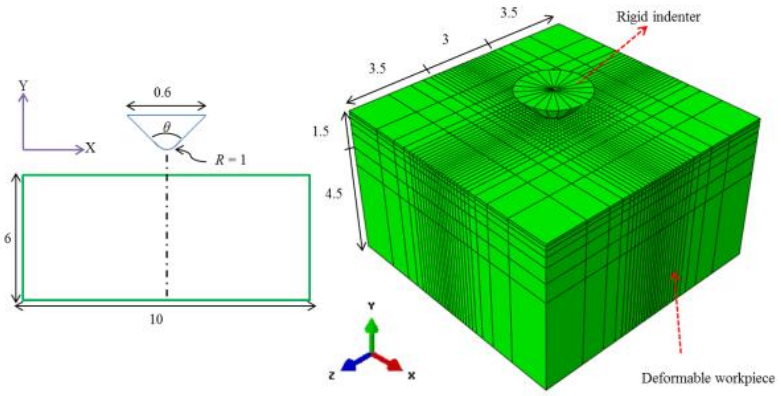

http://dx.doi.org/10.1016/j.commatsci.2013.06.057

Fig3.

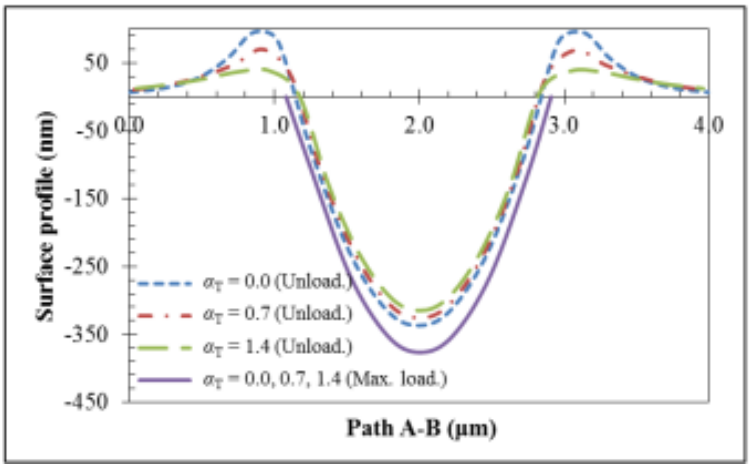

Fig.4

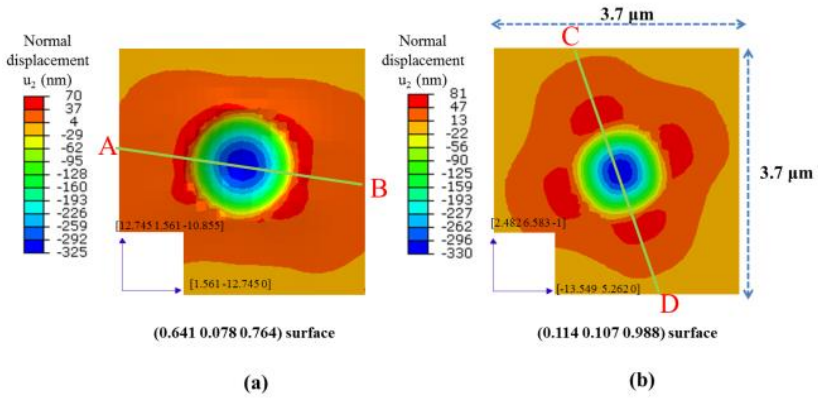

Fig.5

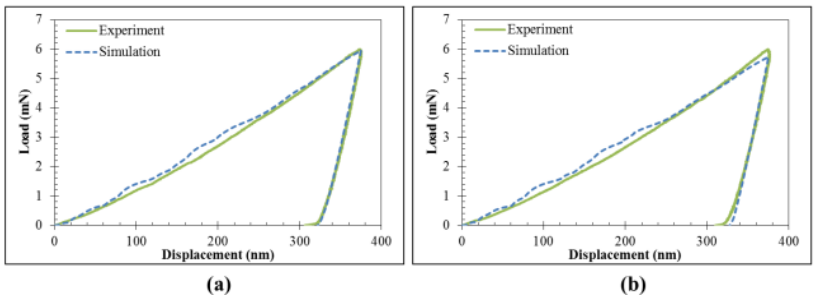

http://dx.doi.org/10.1016/j.commatsci.2013.06.057

Fig.6

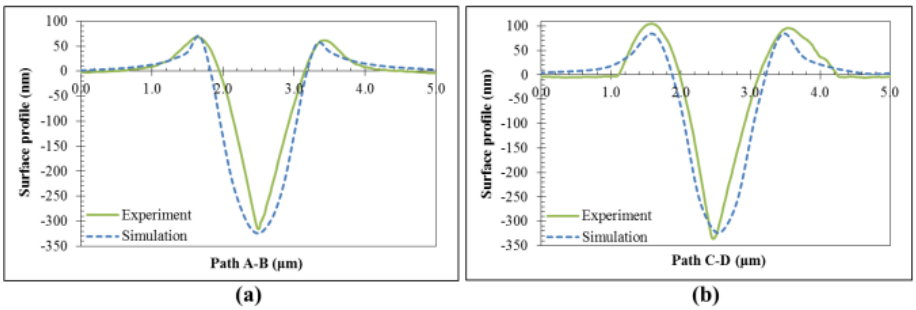

Fig.7

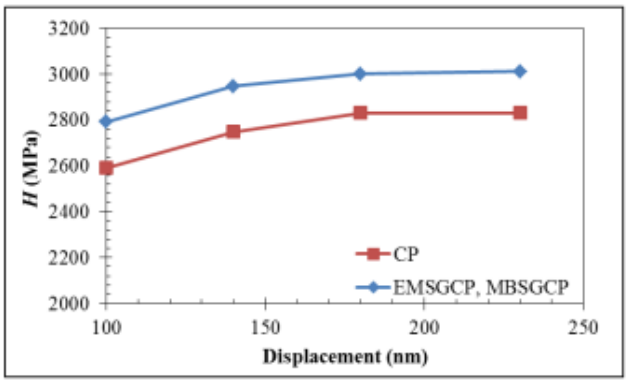

Fig.8

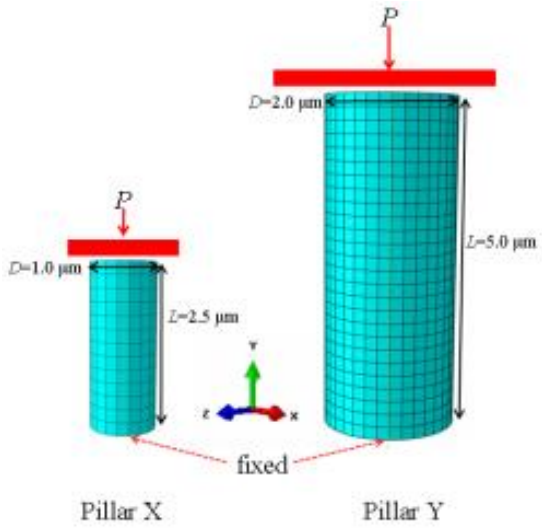

http://dx.doi.org/10.1016/j.commatsci.2013.06.057

Fig.9

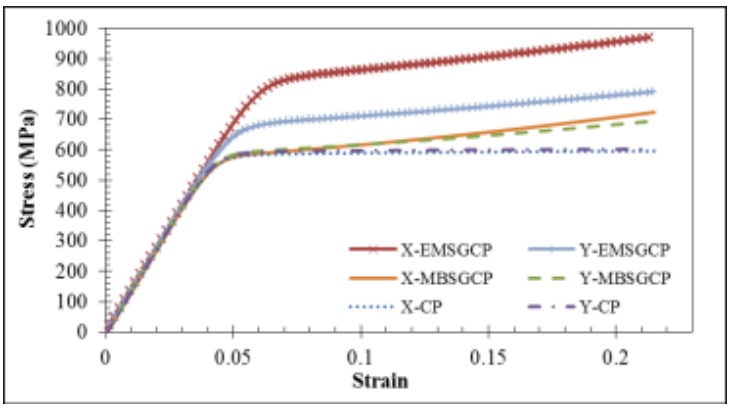

http://dx.doi.org/10.1016/j.commatsci.2013.06.057